Tensile Yield of Polyethylene and Related Copolymers: Mechanical and Structural Evidences of Two Thermally Activated Processes

Valérie Gaucher-Miri and Roland Séguéla*

Laboratoire "Structure et Propriétés de l'Etat Solide", URA CNRS 234, Bât. C6, Université des Sciences et Technologies de Lille, 59655 Villeneuve d'Ascq Cedex, France

Received February 6, 1996; Revised Manuscript Received November 4, 1996[⊗]

ABSTRACT: The true stress−strain characterization of the tensile yield as a function of temperature and cross-head speed is reported for three ethylene−butene copolymers having different crystal weight fractions in the range 0.66−0.35. Evidence is given of two plastic processes operating competitively depending on the experimental conditions. Crystal shear and crystal block sliding are suggested on the basis of the concept of the mosaic block structure of the crystalline lamellae. Small-angle and wide-angle diffraction measurements together with infrared measurements support this conclusion. Two theoretical models of plastic deformation borrowed from solid state physics are proposed to account for our findings. These are a homogeneous crystal slip involving thermal nucleation of dislocations and a heterogeneous crystal slip operating through the defective block boundaries. The competitive action of the two processes which relies on the requirement of the lower energy-consuming pathway of deformation is discussed in terms of a combination between thermal activation and strain-hardening. The proposed models provide an explanation for the major influence of the crystal thickness on the temperature of occurrence of the homogeneous slip. The role of the amorphous phase is discussed in relation to the strain-hardening accompanying the two processes.

Introduction

Polyethylene has been one of the most widely studied semicrystalline polymers as concerns plasticity phenomena owing to its simple crystalline structure and well-characterized physical properties. Besides, owing to its low glass transition temperature, the amorphous phase contributes very little to plastic processes at room temperature or above but rather works in stress transfer and orientation effects. Few tentatives have been made to study the elementary processes of plasticity in the bulk isotropic state because of the complex mixing of orientation and deformation effects in both the crystalline and the amorphous phase.[1−4] WAXS and SAXS analyses during tensile experiments have notably showed that the crystals take a preferred oblique orientation with respect to the deformation direction. The earlier orientation trend of the *a* axis compared to the *b* axis is relevant to the untwisting of the lamellar crystalline ribbons within the spherolites at the onset of plastic deformation.[4] Then, depending on the deformation temperature, lamellar fragmentation alone or associated with chain slip may occur. The more significant contributions to the understanding of plasticity have been obtained from investigations carried out on oriented bulk materials,[5−7] single crystals, or oriented single-crystal mats[8−10] which proved to be model systems for X-ray diffraction and electron microscopy experiments. Overviews on this topic have been reported by Bowden and Young[11] and Lin and Argon.[12] Two main processes of plasticity have been disclosed, namely a coarse slip involving fragmentation of the crystalline lamellae into blocks and a fine slip relevant to a more or less homogeneous shear of the crystal blocks. The orientation of the crystal chain axis aslant with respect to the tensile direction arises from the requirement of a maximum resolved shear stress for the activation of the more compliant slip systems containing the *c* axis.[1,3,9] Martensitic-like phase change and twinning have also been shown to occur, but these processes do not contribute significantly to plastic strain. Both are transitory stages in the crystal approach toward the preferred oblique orientation for slip.[1] At the ultimate stage of the deformation of the spherolites, a fibrillar texture forms with a preferred *c* axis orientation along the deformation direction.

Descriptions of crystalline defects in chain-folded polyethylene crystals in terms of dislocations were reported in the mid sixties.[13,14] In parallel, several authors have theoritically approached the energetic aspect of plastic phenomena in the scheme of classical solid state physics involving crystal slip.[15−17] Borrowing for these studies, a model has been developed for the yield of polyethylene on the basis of the thermal activation of dislocations under the action of an applied stress.[18,19] Several contributions have provided experimental support to the model using data from various kinds of polyethylenes at different draw temperatures.[20−22]

As concerns the amorphous phase contribution in the achievement of plastic deformation, transmission electron microscopy provided valuable qualitative information on the role of the intercrystalline tie molecules and the mechanisms of chain unfolding.[23,24] Infrared spectroscopy also proved to be an efficient tool for quantitative measurement of orientation functions and conformational changes. The transformation of the chain folds into oriented tie molecules between the crystal blocks of the fibrillar texture has been demonstrated.[25−28]

Recently, Argon and co-workers reinvestigated in a systematic way the plastic behavior of high-crystallinity polyethylene in a single-crystal-textured state as well as in the isotropic state, using various deformation modes.[29−32] According to these authors, deformation of the amorphous phase involving lamellar separation and interlamellar sliding are followed by crystal deformation through entirely crystallographic mechanisms. In addition, quite satisfactory simulations of large-strain plastic deformation and texture evolution in the various

[⊗] Abstract published in *Advance ACS Abstracts,* January 1, 1997.

S0024-9297(96)00187-8 CCC: $14.00

Table 1. Weight-Average and Number-Average Molar Weights (M_w and M_n), Ethyl Group Concentration (χ), Weight- and Volume-Fraction Crystallinity (α_c and ϕ_c), and Crystal Thickness (l_c), of the Polymers Studied

materials	$M_w \times 10^{-3}$	$M_n \times 10^{-3}$	χ (ethyl/CH_2 in %)	α_c	ϕ_c	l_c (nm)
PE-2	157	30	0.4_0	0.69	0.65	17.8
PE-4	136	31	1.3_5	0.55	0.51	12.5
PE-6	146	27	3.8_0	0.35	0.32	8.0

testing modes have been made thanks to a micromechanical composite model involving the intrinsic physical characteristics of the effective slip systems.[32] An analogous successful simulation of both plastic behavior and texture changes with strain has been proposed by G'Sell and Dahoun[33] combining crystal plasticity and network contributions.

In a previous publication[34] we reported on the phenomenological aspects of the tensile yielding of polyethylene and related copolymers. The nominal stress−strain curves of a series of ethylene−butene random copolymers under tensile loading exhibited double yield points which changed in shape according to the temperature and the cross-head speed of the experiment. The same features were observed for all materials, but for various experimental conditions. These features were discussed in terms of two thermally activated rate processes of plastic deformation. Brooks *et al.*[35] reported analogous findings from tensile experiments and showed besides, from compressive experiments at room temperature, that the mechanism operating at the first yield point is nearly strain-recoverable while the one which governs the second yield point brings about a truly plastic strain.

The present paper deals with more rational criteria of characterization of the mechanical behavior of polyethylene thanks to the determination of the true stress−strain curves of tensile drawing experiments involving plastic instability. Two quantitative models borrowed from solid state physics are introduced on structural grounds characteristic of semicrystalline polymers.

Experimental Section

Materials. Three industrial-grade ethylene−butene random copolymers having various co-unit contents but nearly similar molecular weights have been investigated. The materials were compression-molded from pellets into sheets about 3 mm thick at 190 °C and slow cooled to room temperature at about 20 °C/min. Table 1 shows the physicochemical characteristics of the materials studied. These materials have been labeled according to our previous[34] study dealing with the phenomenological aspects of double yield in polyethylene and related copolymers.

Thermal Analysis. The materials were studied on a Perkin-Elmer DSC-7 differential scanning calorimeter at a heating rate of 10 °C/min with samples of about 5 mg. The temperature and heat flow scales were calibrated using the melting of high-purity indium and zinc samples. The crystal core weight fractions, α_c, were thus determined from the ratio of the melting enthalpy of the samples to that of a perfect and infinite polyethylene crystal, *i.e.* 290 J/g at the temperature of thermodynamic melting.[36] The baseline under the melting endotherm was drawn linearly between the onset and the end of the melting process. The onset of the melting, which is highly dependent on the crystallinity of the polymers, was determined at the first signs of deviation of the DSC curve from the baseline. The melting enthalpy accuracy was about 5 J/g. The crystal core volume fraction was assessed from the relation

$$\phi_c = \alpha_c \rho / \rho_c \tag{1}$$

where ρ is the density of the material and $\rho_c = 1.000$ g/cm^3 the density of the crystalline phase.[13] The densities of the materials were determined at 23 °C in a water−2-propanol gradient column that was calibrated in the range 1.000−0.900 g/cm^3 thanks to ten hollow glass beads having a density accuracy of 10^{-4}.

Worth mentioning is the broad melting endotherm[34] of the lower crystallinity material that is relevant to a broad crystal thickness distribution due to the well-known chemical heterogeneity of the copolymers issued from Ziegler−Natta catalysis.[37]

X-ray Diffraction. Wide-angle X-ray scattering (WAXS) and small-angle X-ray scattering (SAXS) experiments were performed in photographic mode on a modified Luzzati-Baro goniometer equipped with two pinhole collimators of 0.5 mm in diameter, 200 mm apart. The nickel-filtered Cu Kα radiation of wavelength $\lambda = 0.154$ nm was selected from a Siemens tube operated at 40 kV and 15 mA. The sample-to-film distance was 50 mm and 400 mm for WAXS and SAXS experiments, respectively. The intercrystalline long period, L, of both undeformed and drawn samples was directly computed from the SAXS maximum owing to the Bragg relation. The most probable thickness, l_c, of the crystal cores was then assessed from

$$l_c = L\phi_c \tag{2}$$

which assumes that l_c is small compared to the crystal lateral dimensions.

In the case of four-point SAXS patterns, the orientation of the lamella normal with respect to the draw axis is directly assessed from the azimuth of the diffraction spots. The determination of the chain axis orientation from the WAXS patterns is made using Wilchinsky's relations[38]

$$\langle \cos^2 \psi \rangle_a = \langle \cos^2 \psi \rangle_{200} \tag{3}$$

$$\langle \cos^2 \psi \rangle_b = 1.445 \langle \cos^2 \psi \rangle_{110} - 0.445 \langle \cos^2 \psi \rangle_{200} \tag{4}$$

$$\langle \cos^2 \psi \rangle_c = 1 - \langle \cos^2 \psi \rangle_a - \langle \cos^2 \psi \rangle_b \tag{5}$$

where ψ is either the angle between a given chain axis and the draw direction or the azimuth of the relevant reflection.

Infrared Characterization. Unpolarized infrared (IR) measurements were carried out in transmission mode on the microscope attachment of a Fourier transformed infrared Perkin-Elmer 2000 spectrometer equipped with a narrow-range MCT detector. Dried and CO_2-free air was used to purge the sample compartment. The size of the focused beam on the sample was 100 μm. Every spectrum consisted of 50 scans having a resolution of 4 cm^{-1}. The 150 μm thick samples were drawn at room temperature in an Instron tensile testing machine and subsequently analyzed in the unloaded stated in order to probe the conformational changes due to the sole contribution of the plastic strain. Local IR measurements were carried out as a function of the true plastic strain determined *a posteriori*, owing to ink marks 1.5 mm apart prior to deformation, along samples drawn up to the neck and beyond the neck.

Table 2 shows the assignment of the IR bands[25,39] that have been used for the study of the strain-hardening effect. In order to account for the thinning down of the sample with increasing strain, reduced absorbances A^* were determined from the ratio of the true absorbance of every IR band to that of the 909 cm^{-1} reference band, which is independent of crystallinity and chain conformation.

Tensile Testing. Uniaxial tensile experiments were performed on a screw-driven Instron machine equipped with a video-monitored optical extensometer.[40] A method especially

Table 2. Assignment of the Selected Infrared Bands of Polyethylene

wavenumber (cm^{-1})	phase	assignment
909	C + A	CH_2 wagging in vinyl end grougs
1080	A	skeletal C−C stretching in *t* and *g* conformations
1303	A	CH_2 twisting in *gtg* + *gtg′* conformations
1352	A	CH_2 wagging in *gg* conformations
1368	A	CH_2 wagging in *gtg′* conformations
1894	C	combination of the 1168 cm^{-1} Raman-active mode and the 720 and 730 cm^{-1} infrared out-of-phase and in-phase CH_2 rocking in *t* conformations
2016	C + A	combination of the 1295 cm^{-1} aman fundamental and the 720 and 730 cm^{-1} infrared modes plus combination of the 1303 and the 720 cm^{-1} infrared modes in *t* conformations

[a] *g* = gauche; *t* = trans.

designed for strain determination at a very local scale in strongly necking materials has been used for measuring the longitudinal strain, ϵ_z, and the transverse strains, ϵ_x and ϵ_y, along the width and thickness of the sample, respectively. This method is based on the analysis of the distortions of a linear target drawn aslant to the tensile direction in the narrower region of the hourglass-shaped samples.[41] True stress−strain curves were recorded at various cross-head speeds in the temperature range −20 to +120 °C owing to a temperature-controlled chamber, the regulation of which was done by means of a cooled nitrogen flow below room temperature or electric heaters above room temperature.

The strain-hardening coefficient

$$\gamma = \left(\frac{\partial \ln \sigma}{\partial \ln \lambda}\right)_{\dot{\epsilon}} \qquad (6)$$

was computed from a function-fitting procedure on the true stress−true strain curves, using fifth-order polynomial fits. In this equation, σ is the true stress, $\lambda = 1 + \epsilon_z$ is the draw ratio, and $\dot{\epsilon} = \partial\epsilon_z/\partial t$ is the true strain rate.

The samples were cut out from the compression-molded sheets owing to a cutting die having an hourglass shape in order to enforce necking in a well-localized place of the sample. The sample gauge had a radius of curvature of 58 mm, a length of 50 mm, and a minimum width of 5 mm. The analysis was restricted to a 5 mm long region in the narrower central part of the gauge where the sample width can be considered constant thanks to the very large curvature radius.

Results

True Stress−Strain Experiments. The nominal stress and true longitudinal strain variation curves with time of PE-2 for two draw temperatures of 20 and 80 °C at a cross-head speed of 0.05 mm/min are reported in Figure 1. Following the elastic deformation stage, a necking phenomenon is clearly disclosed at 20 °C by the drop of nominal stress and concomitant rapid increase of local strain rate. However, for 80 °C, the shape of the nominal stress and the true strain curves suggests the occurrence of two plastic regimes, each of them having a proper constant strain rate as judged by the linear variation of the true strain with time. Besides, the significantly lower value of the true strain rate, $\partial\epsilon_z/\partial t$, in the strain range $0.15 < \epsilon_z < 0.5$ compared with that in the range $\epsilon_z > 0.5$, together with the steadily increasing nominal stress in the same strain range, indicates that a homogeneous plastic process takes place between the elastic and necking domains. The corresponding true stress−strain curves of Figure 2 support

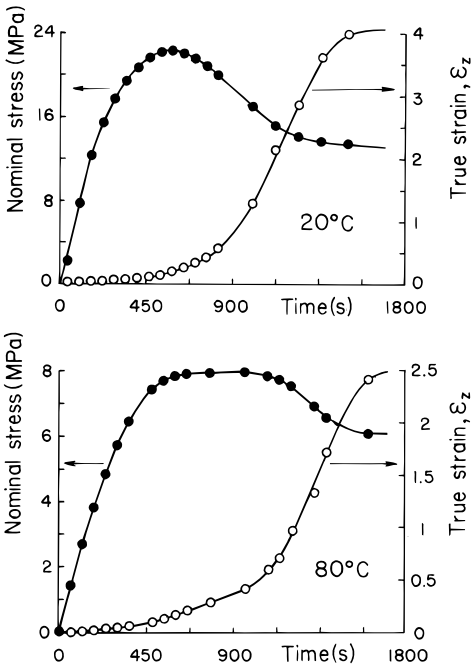

Figure 1. Nominal stress and true strain curves of PE-2 as a function of draw time for the draw temperatures 20 and 80 °C (CHS = 0.5 mm/min).

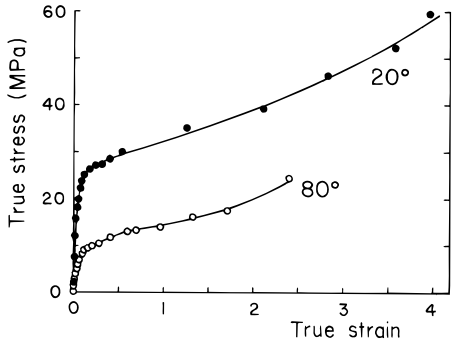

Figure 2. True stress−strain curves of PE-2 for the draw temperatures 20 and 80 °C (data from Figure 1).

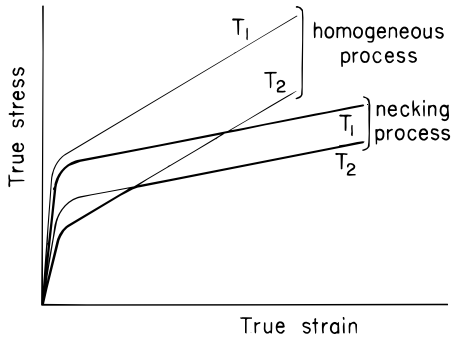

Figure 3. Schematic drawing of the influence of temperature on the contribution of two plastic processes in the shape of the true stress−strain curves ($T_2 > T_1$).

the conclusion of two processes operating consecutively at 80 °C, through the appearance of two yield points at about $\epsilon_z = 0.15$ and $\epsilon_z = 0.6$, while only one occurs at 20 °C. The sketch of Figure 3 is a guideline to show the two kinds of stress−strain curve combinaison leading to the two cases of Figure 2. It assumes that the homogeneous plastic process is more temperature dependent and has a stronger strain-hardening than the necking process. Under such considerations, at the higher draw temperature T_2 (Figure 3), the homoge-

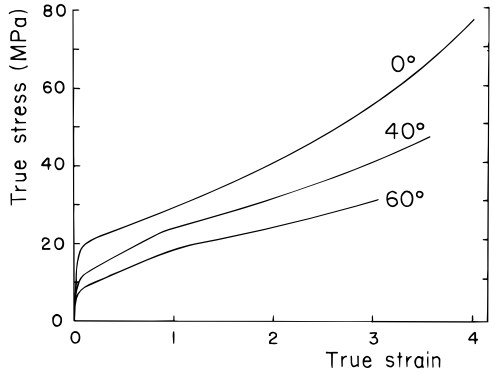

Figure 4. True stress−strain curves of PE-4 for the draw temperatures 0, 40, and 60 °C (CHS = 5 mm/min).

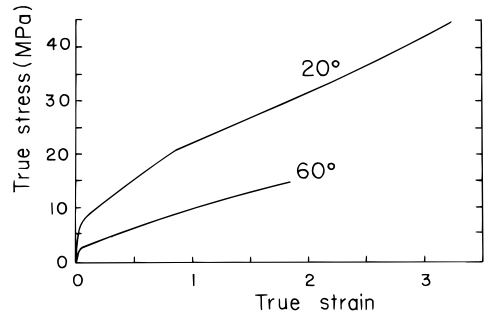

Figure 5. True stress−strain curves of PE-6 for the draw temperatures 20 and 60 °C (CHS = 5 mm/min).

neous process having the lower yield stress is activated first. But as the applied stress increases due to gradual chain tightening, the yield stress of the necking process is reached. Owing to this latter process, the homogeneous process quickly looses activity. At the lower draw temperature T_1 (Figure 3), the homogeneous process now has a higher yield stress than the necking process, so that this later becomes activated first. But, thanks to the lower strain-hardening of the necking process, no opportunity is given for the homogeneous process to become operative.

Similar effects have been observed in the case of PE-4, but for different drawing conditions, as shown on the true stress−strain curves of Figure 4 recorded at the draw temperatures of 0, 40, and 60 °C for a cross-head speed of 5 mm/min. At 40 and 60 °C, a homogeneous stage of plastic deformation with a strong strain-hardening develops prior to necking, in the strain range $0.1 < \epsilon_z < 1.0$. On the contrary, necking occurs readily at about $\epsilon_z = 0.2$ at 0 °C.

Figure 5 shows the true stress−strain curves of PE-6 at the draw temperatures of 20 and 60 °C for a cross-head speed of 5 mm/min. Two yield points appear at 20 °C while a single yield point occurs at 60 °C, followed by homogeneous deformation. In this latter case, the heterogeneous process seems to be readily obliterated.

The strain rate incidence on the development of plastic deformation supports the thermally activated character of the two plastic processes. Figure 6 shows the nominal stress and true strain curves versus time of PE-4 at the cross-head speeds of 5 and 0.05 mm/min for a draw temperature of 20 °C. This figure shows that, for sufficiently low cross-head speed at 20 °C, a clear-cut regime of homogeneous plastic deformation may be activated in the strain range $0.1 < \epsilon_z < 0.7$ prior to the necking process. The corresponding true stress−strain curves of Figure 7 corroborate the change of plastic regime at about $\epsilon_z = 0.7$ for the cross-head speed 0.05

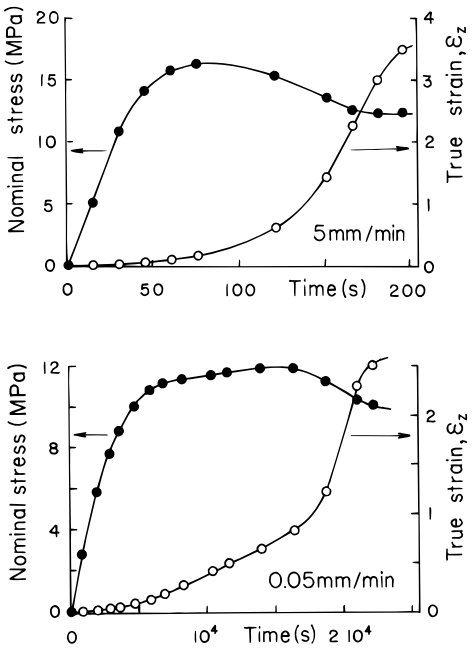

Figure 6. Nominal stress and true strain curves of PE-4 as a function of draw time at the CHS of 5 and 0.05 mm/min for the draw temperature 20 °C.

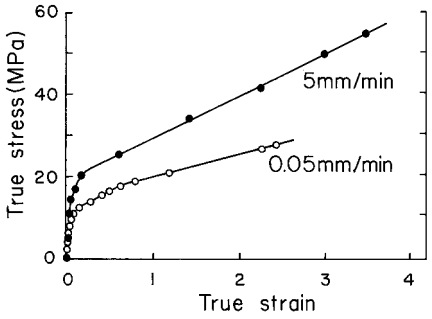

Figure 7. True stress−strain curves of PE-4 for the CHS of 5 and 0.05 mm/min for the draw temperature 20 °C (data from Figure 6).

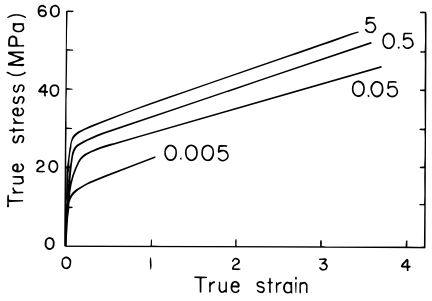

Figure 8. True stress−strain curves of PE-2 at the draw temperature 20 °C for various values of the CHS: 5, 0.5, 0.05, and 0.005 mm/min.

mm/min. A single yield point is observed for the cross-head speed 5.0 mm/min. This reveals the greater strain rate sensitivity of the homogeneous plastic process.

The true stress−strain curves of PE-2 at 20 °C over a three decade range of cross-head speeds are reported in Figure 8. The yield stress gap in the lower decade is twice as large as that in the higher two decades, indicating a stronger thermal activation at low strain rates. This shows that, also for PE-2, the homogeneous process which is favored at low strain rates is more strain rate sensitive than the necking process. It is an additional evidence of the greater thermal activation of

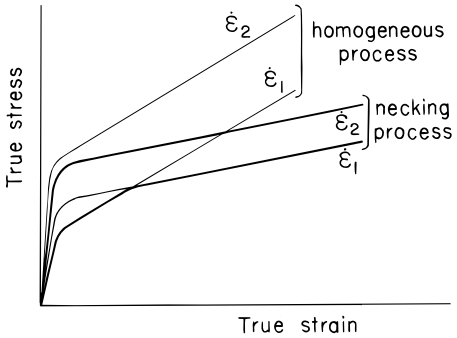

Figure 9. Schematic drawing of the influence of strain rate on the contribution of two plastic processes in the shape of the true stress−strain curves ($\dot{\epsilon}_2 > \dot{\epsilon}_1$).

the homogeneous process already disclosed by the temperature dependency.

Figure 9 is a sketch of the combinaison of the two processes for two different strain rates, assuming a higher strain rate sensitivity and a stronger strain-hardening for the homogeneous plastic process. In the case of the lower strain rate, $\dot{\epsilon}_1$, the homogeneous process proceeds first but the competition with the necking process turns in favor of the latter when the stress−strain curves cross together, making the necking process energetically less costly. For the higher strain rate, $\dot{\epsilon}_2$, the necking process is always more favorable than the homogeneous process.

At low temperature or high cross-head speed, the heterogeneous necking process occurs first but seems to be accompanied by the homogeneous process as judged by the rather slow drop of the nominal stress after the yield point. As a matter of fact, thanks to its high strain rate sensitivity, the homogeneous process may not occur first but may proceed along with the necking process at a much lower strain rate than the overall one in order to adjust its own flow stress to that of the leading necking process. Thereby, the homogeneous process occurs as a secondary creeplike phenomenon. But, as strain increases, it should gradually reduce its strain rate, because of its strong strain-hardening, until only the necking process remains active.

Conversely, at high temperature or low cross-head speed, the homogeneous process is more favorable than necking. This latter process may nevertheless be activated after the applied stress has reached its own yield stress. In spite of the lower strain-hardening of the necking process, the homogeneous process may continue to proceed for a while at a gradually decreasing strain rate in order to adjust its own flow stress to the stress level imposed by the preferred necking process, until exhaustion.

The macroscopically heterogeneous nature of the necking process, otherwise plastic instability, suggests that the basic mechanism is a microscopically heterogeneous one, *i.e.* a heterogeneous or localized crystal slip. In this instance, worth mentioning is Peterlin's description of macroscopic necking as a result of gathering of microscopic neck processes at the scale of the individual crystalline lamellae.[3] Conversely, the macroscopically homogeneous plastic process could be ascribed to a microscopically homogeneous plastic mechanism, namely a homogeneous crystal slip leading to uniform crystal shear.

The variation curves as a function of strain of the strain-hardening rate of PE-4 are reported in Figure 10 for the draw temperatures of 0 and 40 °C. These plots

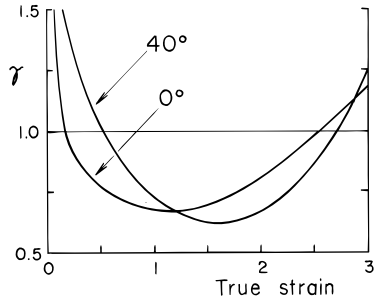

Figure 10. True strain-hardening rate, $\gamma = \partial \ln \sigma / \partial \ln \lambda$, as a function of strain for PE-4 at 0 and 40 °C (CHS = 5 mm/min).

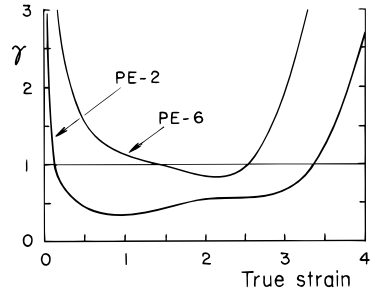

Figure 11. True strain-hardening rate, $\gamma = \partial \ln \sigma / \partial \ln \lambda$, as a function of strain for PE-2 and PE-6 at 20 °C (CHS = 0.5 mm/min).

show that the instability criterion, $\gamma < 1$, is only fulfill for $\epsilon_z > 0.6$ at 40 °C, *i.e.* in the strain range of the necking process as previously judged from Figure 4. Oppositely, at 0 °C, deformation becomes heterogeneous as soon as $\epsilon_z = 0.2$, that is the strain threshold of the necking process at this temperature (Figure 4). Similar observations can be made from Figure 11, which displays the strain-hardening variations with strain of PE-2 and PE-6 at 20 °C. Indeed, $\gamma < 1$ for $\epsilon_z > 0.2$ in the case of PE-2 indicates that necking takes place without substantial homogeneous deformation as previously concluded from Figure 2. In the case of PE-6, $\gamma > 1$ for $\epsilon_z \leq 1.2$ is consistent with the conclusion from Figure 5 that homogeneous deformation precedes heterogeneous deformation.

The variation curves of the true strain-hardening rate do not allow observation of the subtile changes of variation of the slope of the true stress−strain because of the bluring effect of the ln λ strain parameter that compresses the strain scale at large values. Besides, the fitting procedure on the true strain−stress curve that is used for the calculation of the strain-hardening rate has an additional smoothing effect on the changes of slope. So, the experimental slope $\partial\sigma/\partial\epsilon_z$ has been used for discussing the strain-hardening effect. Figure 12 shows the variation of the slopes of the true stress−true strain curves as a function of the draw temperature for the linear domains of the two regimes of plastic deformation. It clearly appears that the necking process has a lower strain-hardening rate than the homogeneous process, in agreement with our previous interpretation of the true stress−true strain data.

X-ray Diffraction Characterization. Combined wide-angle and small-angle X-ray diffraction experiments have been performed in order to bring additional information on the respective contributions of the two plastic processes.

Figure 13 shows the WAXS and SAXS patterns as a function of strain of PE-4 for the draw temperature of 20 °C. In the range of plastic strain $\epsilon_z \leq 1.3$, the gradual buildup of a four-point SAXS pattern is relevant to the

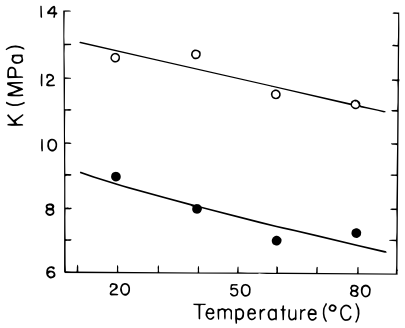

Figure 12. Experimental strain-hardening rate, $K = \partial\sigma/\partial\epsilon_z$, of PE-4 as a function of the draw temperature for (○) the DN process and (●) the BS process (CHS = 0.5 mm/min).

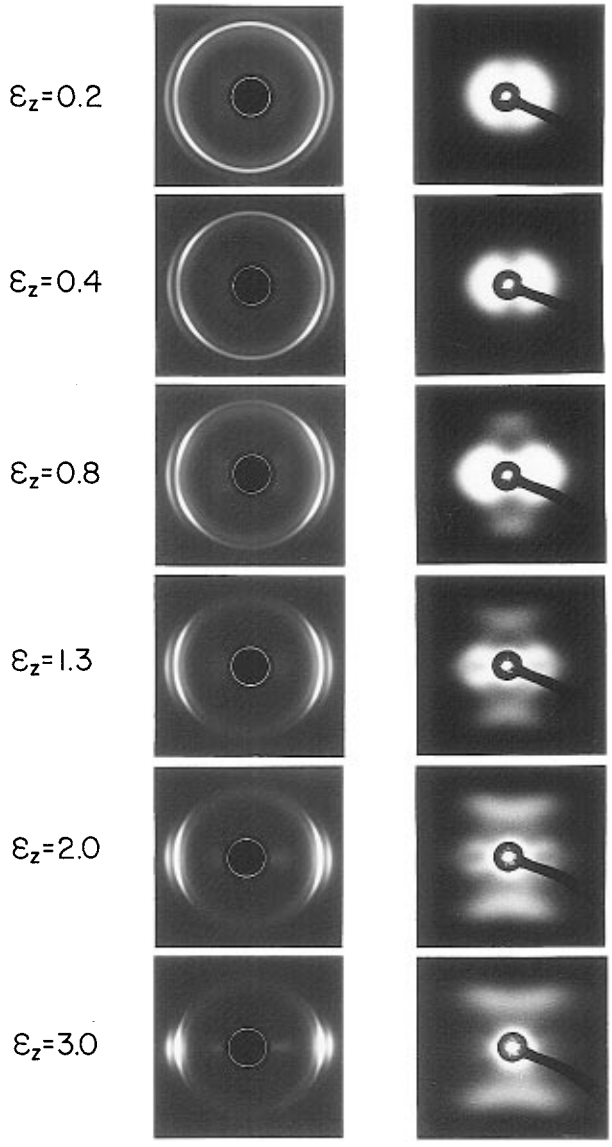

Figure 13. WAXS and SAXS patterns of PE-4 as a function of plastic strain for the draw temperature 20 °C at a CHS of 0.5 mm/min.

rotation of the crystalline lamellae toward a preferred orientation for slip. At $\epsilon_z = 1.3$, the orientation of the normal to the lamella surface makes an angle of 50 ± 1° with respect to the draw direction. From the WAXS pattern, the polar angle of the chain axis at the same strain is 33 ± 1°, indicating a significant chain tilt that supports the homogeneous slip proposal. The appearance of a faint two-point meridional diffraction in addition to the strong four-point diffraction on the SAXS patterns as soon as $\epsilon_z = 0.4$ reveals that heterogeneous slip accompanied with lamella fragmentation begins to take place before the occurrence of the second yield point leading to partial transformation of the material into a fibrillar structure. However, the weak intensity of this pattern shows that the heterogeneous slip is still of little contribution at this stage of the deformation. This is in line with the conclusion from the mechanical study that the heterogeneous process begins to contribute to the plastic deformation before the second yield point, but at a much lower strain rate than the homogeneous process. With increasing strain beyond the second yield point, *i.e.* for $\epsilon_z \geq 1.3$, the two-point meridional diffraction increases in intensity at the expense of the four-point diffraction as a result of the gradual transformation of the inclined lamellae into fibrils oriented parallel to the draw axis. At $\epsilon_z = 3.0$, all the material has turned into a fibrillar structure.

The preferred orientation of the crystalline lamellae at low strains, as evidenced from the SAXS patterns of Figure 13, is relevant to a rotation of the chain axis toward a direction for which a maximum value of the resolved shear stress in a favorable slip plane is reached, *i.e.* at an angle of about 45° with respect to the draw direction. In this connection, the systematic conclusion by Argon and co-workers,[29−31] from various kinds of deformation experiments, that the mainly active slip system at the early stage of plasticity in textured high-crystallinity polyethylene at room temperature is the (100)[001] system having the lower critical shear stress is an evidence for the requirement of a lower energy pathway of deformation. Notwithstanding, the steady concentration of the outer (200) reflection on the equator of the WAXS patterns of Figure 13 clearly indicates that the (100) planes orient themselves parallel to the draw axis. They are not therefore in the right orientation for slip in spite of their higher intrinsic compliance. From the evolution of the innermost (110) reflection into quadrant diffractions, one can deduce that the (010) planes are preferentially oriented with their normal at about 50° from the draw axis, indicating that the (010)-[001] chain slip lies in the required position for being the preferred active slip system. This orientation trend is commonly observed in tensile drawing of isotropic spherulitic polyethylene at temperatures in the range 20−60 °C. Worth noticing is the late but sharper orientation of the (110) plane normals compared with the (200) ones. This is relevant to a delayed but faster rotation of the crystalline lamellae about their own *a* axis, as proposed by Kawai *et al.*,[42,43] who have carefully studied and modeled the orientation behavior of spherulitic polyethylene in tensile deformation. The preferred orientation of the (010) planes toward a direction of maximum resolved shear stress, instead of the more compliant (100) planes, suggests that the driving force to the crystalline axis tilting depends more on the energy barrier to the rotation of the rigid twisted lamellae embedded in a rubbery amorphous phase about their long dimension than on the barrier to the activation of crystal slip. Besides, the (010) planes have a much shorter length than the (100) planes since they are perpendicular to the growth *b* direction of the lamellae; hence they are much prone for slip than the extensively long and twisted (100) planes.

Beyond $\epsilon_z = 1.3$, the gradual concentration of the (110) reflection on the equator in addition to the previous equatorial position of the (200) reflection indicates that

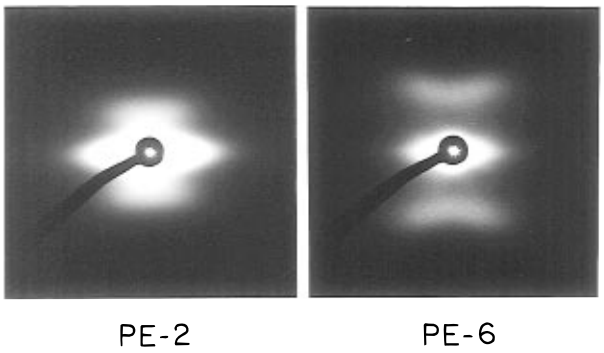

Figure 14. SAXS patterns of PE-2 and PE-6 fibers drawn at 20 °C up to $\epsilon_z = 5.0$ and $\epsilon_z = 4.0$, respectively (CHS of 0.5 mm/min).

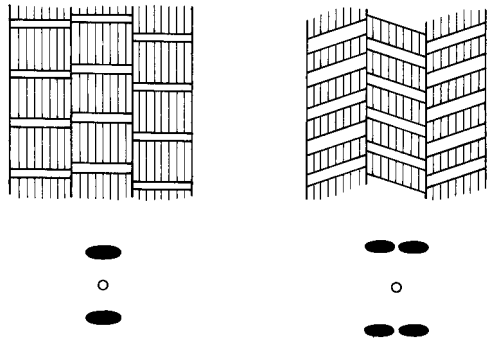

Figure 15. Fiber structures corresponding to the SAXS patterns of Figure 14.

the stretching and unfolding of the chains tilt the chain axis toward the draw direction.

We have shown in a previous study that the low-crystallinity copolymer PE-6 displays a faster orientation trend than the high-crystallinity copolymer PE-2, which has been ascribed to a reduced steric hindrance for the rotation of the lamellae as their dimensions regress.[44] This is in perfect agreement with the above statement about the influence of the crystal lamellae geometry on the orientation trend.

The SAXS fiber patterns of PE-2 and PE-6 drawn at 20 °C, which are reported in Figure 14, display a two-point and a four-point diffraction, respectively. This indicates that the crystal blocks in the fibrils are respectively unsheared and sheared, as displayed in the pictures of Figure 15. Considering that the heterogeneous slip and the homogeneous slip are respectively the prevailing processes in PE-2 and PE-6 at 20 °C, the observed SAXS patterns indicate that the fiber structure has a memory effect of the yielding pathway. In addition, the strong equatorial scattering in the case of PE-2 is relevant to an interfibrillar microvoiding, which corroborates the occurrence of the lamellar fragmentation accompanying micronecking.

Infrared Conformational Analysis. In order to follow the conformational changes in the amorphous phase accompanying the plastic deformation of the crystallites, reduced absorbance measurements were carried out on PE-4 drawn at room temperature at a cross-head speed of 0.05 mm/min. Figure 16 shows the variation with draw ratio of the reduced absorbances of the 1080, 1303, 1352, and 1368 cm^{-1} amorphous bands, together with the 1894 cm^{-1} crystalline band and the 2016 cm^{-1} overall band. The 1303, 1352, and 1368 cm^{-1} bands indicate that an increase of the concentration of the *gg*, *gtg*, and *gtg′* conformations takes place upon deformation in the low strain range corresponding

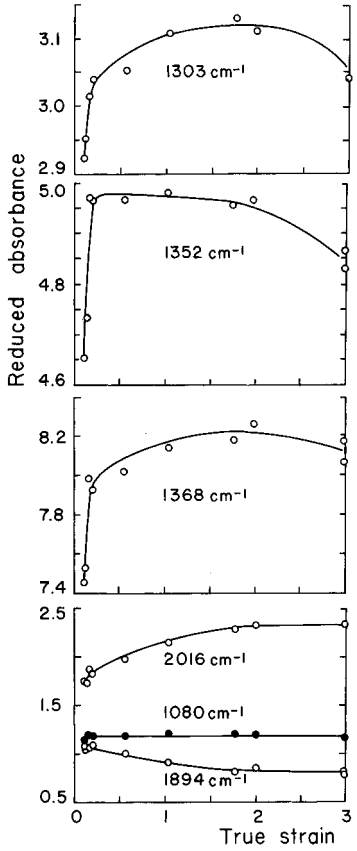

Figure 16. Reduced absorbances of the infrared bands as a function of draw ratio, after unloading, for a PE-4 sample drawn at 20 °C at a CHS = 0.05 mm/min.

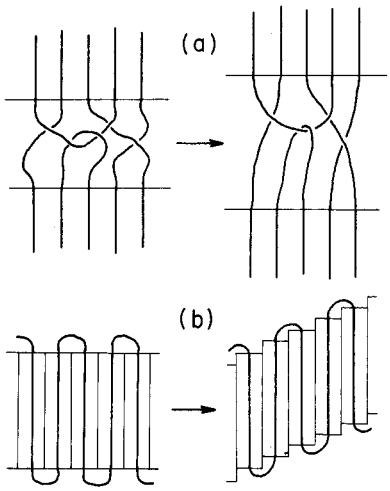

Figure 17. Molecular sketch of the conformational changes in the amorphous phase accompanying (a) the lamellae separation and (b) the homogeneous slip of the crystalline lamellae.

to the homogeneous slip. On the other hand, the 1894 cm^{-1} band reveals a decrease of the concentration of the crystalline *t* conformations while the 2016 cm^{-1} band discloses an increase of the overall *t* conformation concentration. These results entail, first of all, that isolated *g* conformations gradually disappear as the amorphous phase is strained. Secondly, they mean that topological constraints involving associations of *g* conformations build up within the amorphous chains in the homogeneous deformation stage. Figure 17 shows an attempt to account for these conformational constraints. It worth mentioning that the situations depicted in this

figure are based on the fact that the preferred (010)-[001] chain slip is essentially perpendicular to the chain folds, the chain folding being indeed predominant in the (100) for melt-crystallized polyethylene.[45] The first point is that isolated *g* conformations may disappear in the taut portions of the chain loops and intercrystalline tie molecules thanks to the energetically favorable $g \rightarrow t$ isomerization (Figure 17a). Secondly, owing to their rather bent shape,[26] the *gg* and *gtg* conformations are rather likely to occur at the knots of entangled loops which act as stress transfer agents between the crystallites (Figure 17a), as well as in the short chain folds that bridge the slip planes and that are straightened by the homogeneous slip (Figure 17b), involving great conformational constraints about the anchoring points. This situation occurs in any lamella undergoing crystal slip, irrespective of chain orientation. Third, the *gtg′* conformations having a rather extended shape should preferentially develop in the tie molecules via the enlacements with the neighbor chains that are likely to generate kink defects (Figure 17a). But as soon as block sliding occurs, chain unfolding entails a $g \rightarrow t$ isomerization of the *g*-rich conformation associations belonging to the chain folds and intertwined tie molecules. This effect is clearly disclosed by the significant drop of the reduced absorbances of the 1303, 1352, and 1368 cm^{-1} bands. It is worth noticing that the strain threshold for the drop of the *g* conformations, $\epsilon_z \approx 1.8$, is somewhat greater than that of the heterogeneous plastic deformation, $\epsilon_z = 0.8$ (see Figure 6), since the heterogeneous slip process is sufficiently advanced to involve a detectable amount of unfolded chains compared to the remaining unaffected chains.

The decrease of the concentration of the crystalline *t* conformations relevant to the reduced absorbance of the 1894 cm^{-1} band (Figure 16) cannot be ascribed to crystallinity variations as judged from the quite constant melting enthalpy in the strain range $0 < \epsilon_z < 5$. Besides, the invariance of the reduced absorbance of the 1080 cm^{-1} amorphous band is consistent with a constant amorphous content. An issue for this finding is that numerous conformational defects develop in the crystalline lamellae as a result of the nucleation of dislocations as will be discussed in the next section.

Discussion

Structural Considerations. The whole set of experimental data suggests that, whatever the crystallinity of the material, two plastic processes operate competitively. The quite clear partitioning of the strain scale into two ranges of activity of these two processes entails that they are allowed to proceed independently. This is a necessary condition for them to take place at different true strain rates for a given cross-head speed. This is a strong indication that the two processes operate within well distinct areas of the crystalline phase. We have previously put forward[34] a model in relation to the mosaic structure of the crystalline lamellae, that is sketched in Figure 18. The defective regions between the crystallographically coherent blocks are assumed to be the locus of a sliding of these blocks, namely a heterogeneous slip, while the cores of the crystal blocks are prone to undergo a more or less uniform shear due to a homogeneous slip. This structural model has been borrowed from X-ray diffraction studies reported by Peterlin and Meinel,[3] Kawai *et al.*,[42,43] Takayanagi *et al.*,[6] and Young *et al.*[7] The latter authors notably proposed a coarse slip and a fine slip

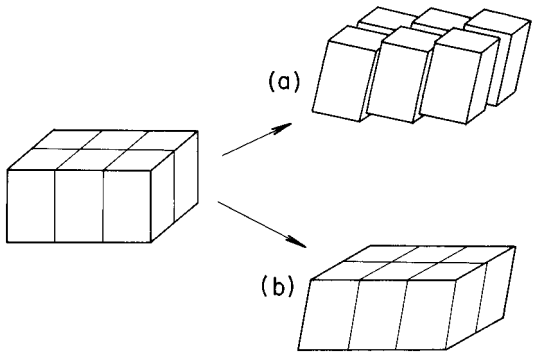

Figure 18. Structural model for the two thermally activated processes of plastic deformation in the mosaic crystalline lamellae: (a) sliding of blocks at the defective boundaries and (b) shear of the crystal blocks.

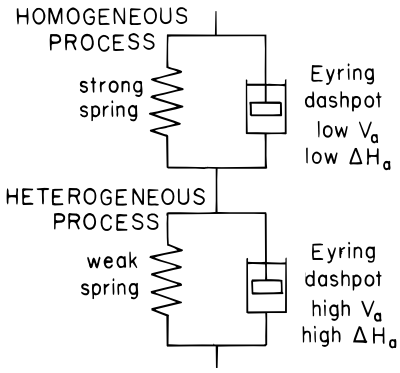

Figure 19. Mechanical model for the two thermally activated plastic processes.

but did not indicate specific locations for each of them. Conversely, Takayanagi *et al.* suspected the paracrystalline structure of the crystallites to be responsible for the occurrence of the two processes.

Mechanical Considerations. The location of the two processes into two distinct areas within the crystals implies that they operate in series association. Indeed, the uniform distribution of the stress over the different regions allows the two processes to be activated selectively according to their critical resolved shear stress (CRSS) and their thermal activation parameters.

A corollary to the series-association model is that the σ versus log $\dot{\epsilon}$ plot should ideally consist of two linear domains, the slope in the range of high strain rate being the lower one.[46] Experimental data of Figure 8 perfectly support this requirement.

Figure 19 shows the corresponding mechanical model of two Voigt elements, each of them consisting of a rubber-like spring in parallel with a thermally activated Eyring dashpot.[47] The dashpot associated with the homogeneous slip has a lower activation enthalpy, ΔH_a, and a lower activation volume, V_a, than the dashpot associated with the heterogeneous slip, *i.e.* greater temperature and strain rate sensitivities. Besides, the spring is stiffer in the case of the homogeneous slip.

Several authors[32,33,48−50] have developed constitutive equations for the plastic flow of semicrystalline polymers, separating the strain and strain rate dependencies of the plastic flow stress into two independent contributions. The additive form, which supports the series model, turned out to be the better expression for the draw stress

$$\sigma(\epsilon_z,\dot{\epsilon},T) = \sigma^*(\dot{\epsilon},T) + \sigma_i(\epsilon_z,T)$$

where σ^* is the effective stress for plastic flow and σ_i is the internal stress that accounts for the strain-hardening of the material. In the present case, the rubber springs of the two Voigt elements of Figure 19 hold for the stretching of the network, which allows both elastic and partial long-term recovery of the deformation. But according to the structural model, the mode of deformation of the amorphous phase should be different for the two slip processes. Indeed, homogeneous slip involves stretching of the chain folds and chain loops that bridge the slip planes. Conversely, heterogeneous slip is accompanied by chain unfolding from the defective interfaces. This latter process involves a much lower number of planes and a much greater chain extension than the former one. Consequently, the spring associated with the homogeneous slip should be much stiffer than the one associated with the heterogeneous slip. Modeling the two kinds of strain-hardening in terms of rubber elasticity is however a very difficult task because of the lack of quantitative information on the chain topology relevant to each of the slip processes.

Proposed Slip Models. The model of plastic yielding of semicrystalline polymers through the nucleation of screw dislocations parallel to the chain axis seems to be adequate for featuring of a *homogeneous slip phenomenon*. The tensile flow stress is given by the equation[19]

$$\sigma_{DN} = \frac{\mu b}{\pi r_0} \exp\left(-\frac{2\pi\Delta G}{\mu b^2 l_c} - 1\right) \tag{7}$$

which involves the following two assumptions: (1) the resolved shear stress operating on the glide planes is maximum, *i.e.* crystal slip occurs at an angle of 45° with respect to the tensile axis, and (2) a uniform distribution of the strain on the crystalline and amorphous phases is obeyed. In eq 7, μ is the shear modulus of the (010) planes involved in the slip process as shown from WAXS, b is the Burgers vector, $r_0 = 1.0$ nm is the core radius of the dislocation, l_c is the crystal thickness, and ΔG is the energy barrier for the dislocation nucleation. For experiments performed at reasonable time scale, ΔG should be about 40 kT, k being the Boltzmann constant and T the absolute temperature. The Burgers vector is taken as half the crystallographic parameter in the chain direction; this is the elementary chain translation afforded through a 180° chain twist, which is the easiest crystalline stem motion.[51]

We have already shown that this model can fairly account for the tensile yielding at 60 °C of a series of ethylene−butene copolymers over a wide range of composition, and crystallized from the melt as well as from solutions of various concentrations.[22]

In an approach of the yield behavior of glassy polymer, Escaig[52] proposed a mechanism of slip of corrugated surfaces due to the lack of crystallographic planes in the amorphous state which can account for the *heterogeneous slip process*. This model was borrowed from the one previously proposed by Friedel[53] for the plasticity of metallic glasses at low temperatures, and which assumes a major activity of stacking faults over dislocations. In this model, the tensile flow stress for trailing the stacking fault is given by the relation[52]

$$\sigma \approx \mu(h/d)^2 \tag{8}$$

where μ is the shear modulus of the slip planes, h is the height of the staking fault normal to the shear interface, and d is the length of the defect in the shear direction.

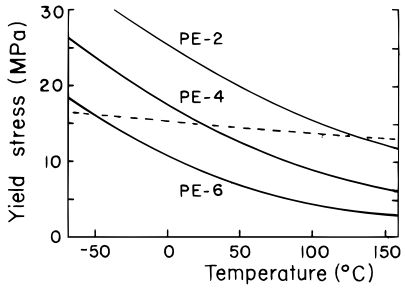

Figure 20. Predicted variation curves of the yield stress for the two models of plastic deformation: (—) homogeneous slip within the crystalline blocks for the three copolymers according to eq 7 and (- - -) heterogeneous slip through the defective boundaries according to eq 9 .

The analogy of this deformation mechanism with the present instance of sliding of crystalline blocks relies on the stacking faults in the mosaic block structure of the crystal lamellae and the concomitant hindrance for dislocation motion within the blocks at temperatures below the α relaxation. From the length of the 2g1 chain kinks that most probably compose the defective interface between the mosaic blocks,[13] a value $d \approx 1.0 \pm 0.2$ nm corresponding to 8 methylene units can be assessed for the extent of the stacking fault in the direction of the chain axis. The value of the stacking fault height can be approximated to the transverse displacement of the planar chain segments adjacent to each 2g1 kink,[13] *i.e.* $h \approx 0.07 \pm 0.01$ nm. Then, thanks to the variation with temperature of the (010) shear modulus,[17] the following equation can be derived for the flow stress temperature dependency of the block sliding process:

$$\sigma_{BS}\,(\text{MPa}) \approx 21.6 - 2.85 \times 10^{-2}T + 1.96 \times 10^{-5}T^2 \tag{9}$$

The variation curves of the yield stress as a function of temperature predicted from the models for the homogeneous and heterogeneous slip processes, σ_{DN} and σ_{BS}, respectively, are compared in Figure 20. The three curves $\sigma_{DN}(T)$ account for the incidence of the different crystal thicknesses of the three copolymers on the homogeneous slip while a unique curve $\sigma_{BS}(T)$ holds for the heterogeneous slip. This latter only roughly accounts for the experimental data of Figures 1 and 2 because the model is a very simple approximation of the real phenomenon of heterogeneous slip. The main feature of Figure 20 is that σ_{DN} is much more temperature-dependent than σ_{BS} because the additional temperature dependency of the dislocation nucleation energy barrier over that of the shear modulus which contributes into both models. Moreover, the predicted values of the yield stress fairly agree with the measured values. Below the critical temperature of the crossing of the σ_{DN} and σ_{BS} curves, for each copolymer, heterogeneous slip is more favorable than homogeneous slip. Above the critical temperature, homogeneous slip is preferred. This is perfectly consistent with our conclusion from the true stress−strain experiments that the change of yielding behavior with temperature results from the greater thermal activation of the homogeneous process compared with the heterogeneous process. Besides, the critical temperature drops with decreasing

crystal thickness as actually observed on the nominal stress−strain curves.[34]

Strain-Hardening. The infrared data suggest that the chain folds that bridge the slip planes are stressed in various ways depending on the deformation mode (Figure 16). On the one hand, the homogeneous slip involves the straining of a considerable number of folds, because waves of numerous dislocations are activated simultaneously over every crystal block. These folds have a limited extensibility in relation to their short contour length, their anchoring points onto the surface of the crystal blocks working as permanent physical cross-links. The amorphous layer is thus expected to bring about a mechanical contribution similar to that of a deeply intertwined rubber network with a Langevin-type behavior. It results that $\partial\sigma/\partial\epsilon_z$ should be high. On the other hand, the heterogeneous slip is only concerned with the chain folds and chain loops bridging the defective boundaries between the sliding blocks. These folds and loops unfold from the slip interface of the crystal blocks with a great local extension, their anchoring points onto the crystal surface being no longer permanent but transient physical cross-links. In this case, the amorphous layer is expected to behave like a loosely entangled rubber network of the Gaussian type. It entails that $\partial\sigma/\partial\epsilon_z$ should be rather low. This difference in the strain-hardening of the two processes is the second basic element which governs their occurrence, after the thermal activation behavior.

Conclusion

This paper shows that polyethylene and ethylene copolymers may display either homogeneous or heterogeneous deformation under tensile testing, the activation of which is governed by the temperature and strain rate conditions. Homogeneous and heterogeneous slip processes are suggested to be responsible for the two kinds of macroscopic deformation regimes. The stronger thermal activation of homogeneous slip makes it become more favorable than heterogeneous slip as temperature increases and strain rate slows down. The heterogeneous slip may be however activated as deformation proceeds owing to its lower strain-hardening.

Crystal thickness plays a major role in the activation of the two processes. For given experimental conditions, the thinner the crystals, the more favorable is the homogeneous slip. This finding is of prime importance for the understanding of the use properties of ethylene copolymer, such as puncture or tear resistance as well as stress-cracking resistance, which rely on the ability of the materials to develop a ductile mechanism of deformation (*i.e.* homogeneous slip) instead of a brittle mechanism (*i.e.* heterogeneous slip) which promotes crazes and cracks.

References and Notes

(1) Frank, F. C.; Keller, A.; O'Connor, A. *Philos. Mag., Ser. 8* **1958**, *3*, 64.
(2) Meinel, G.; Morosoff, N.; Peterlin, A. *J. Polym. Sci., Polym. Phys. Ed.* **1970**, *8*, 1723.
(3) Peterlin, A.; Meinel, G. *Makromol. Chem.* **1971**, *142*, 227.
(4) Matsuo, M.; Hirota, K.; Fujita, K.; Kawai, H. *Macromolecules* **1978**, *11*, 1000.
(5) Robertson, R. E. *J. Polym. Sci., Polym. Phys. Ed.* **1971**, *9*, 1255.
(6) Takayanagi, M.; Kajiyama, T. *J. Macromol. Sci., Phys.* **1973**, *B8*, 1.
(7) Young, R. J.; Bowden, P. B.; Ritchie, J.; Rider, J. G. *J. Mater. Sci.* **1973**, *8*, 23.
(8) Kiho, H.; Peterlin, A.; Geil, P. H. *J. Appl. Phys.* **1964**, *35*, 1599.
(9) Peterlin, A.; Sakaoku, K. *J. Appl. Phys.* **1967**, *38*, 4152.
(10) Petermann, J.; Gleiter, H. *J. Polym. Sci., Polym. Phys. Ed.* **1973**, *11*, 359.
(11) Bowden, P. B.; Young, R. J. *J. Mater. Sci.* **1974**, *9*, 2034.
(12) Lin, L.; Argon, A. S. *J. Mater. Sci.* **1994**, *29*, 294.
(13) Wunderlich, B. *Macromolecular Physics: Crystal Structure, Morphology and Defects*; Academic Press: New York, 1973; Vol. 1, Chapter 4.
(14) Schultz, J. *Polymer Materials Science*; Prentice Hall: Englewood Cliffs, NJ, 1974; Chapter 2.
(15) Eshelby, J. D.; Stroh, A. N. *Philos. Mag.* **1951**, *42*, 1401.
(16) Peterson, J. M. *J. Appl. Phys.* **1968**, *39*, 4920.
(17) McCullough, R. L.; Peterson, J. M. *J. Appl. Phys.* **1973**, *44*, 1224.
(18) Young, R. J. *Philos. Mag.* **1974**, *30*, 85.
(19) Shadrake, L. G.; Guiu, F. *Philos. Mag.* **1979**, *39*, 785.
(20) Young, R. J. *Mater. Forum* **1988**, *11*, 210.
(21) Crist, B.; Fisher, C. J.; Howard, P. R. *Macromolecules* **1989**, *22*, 1709.
(22) Darras, O.; Séguéla, R. *J. Polym. Sci., Polym. Phys. Ed.* **1993**, *31*, 759.
(23) Petermann, J.; Kluge, W.; Gleiter, H. J. *J. Polym. Sci., Polym. Phys. Ed.* **1979**, *17*, 1043.
(24) Tarin, P. M.; Thomas, E. L. *Polym. Eng. Sci.* **1979**, *19*, 1017.
(25) Glenz, W.; Peterlin, A. *J. Macromol. Sci., Phys.* **1970**, *B4*, 473.
(26) Tagawa, T.; Tabuchi, T.; Kashima, M.; Kobayashi, K. *J. Macromol. Sci., Phys.* **1974**, *B10*, 331.
(27) Hosada, S. *Makromol. Chem.* **1984**, *185*, 787.
(28) Dupuis, J.; Legrand, P.; Séguéla, R.; Rietsch, F. *Polymer* **1988**, *29*, 626.
(29) Bartczak, Z.; Cohen, R. E.; Argon, A. S. *Macromolecules* **1992**, *25*, 4692.
(30) Bartczak, Z.; Argon, A. S.; Cohen, R. E. *Macromolecules* **1992**, *25*, 5036.
(31) Galeski, A.; Bartczak, Z.; Argon, A. S.; Cohen, R. E. *Macromolecules* **1992**, *25*, 5705.
(32) Lee, B. J.; Argon, A. S.; Parks, D. M.; Ahzi, S.; Bartczak, Z. *Polymer* **1993**, *34*, 3555.
(33) G'Sell, C.; Dahoun, A. *Mater. Sci. Eng.* **1994**, *A175*, 183.
(34) Séguéla, R.; Darras, O. *J. Mater. Sci.* **1994**, *29*, 5342.
(35) Brooks, N. W.; Duckett, R. A.; Ward, I. M. *Polymer* **1992**, *33*, 1872.
(36) Wunderlich, B. *Macromolecular Physics: Crystal Melting*; Academic Press: New York, 1980; Vol. 3, Chapter 8.
(37) Schouterden, P.; Vandermarliere, M.; Riekel, C.; Koch, M. H. J.; Groeninckx, G.; Reynaers, H. *Macromolecules* **1989**, *22*, 237.
(38) Wilchinsky, Z. W. *J. Polym. Sci., Polym. Phys. Ed.* **1968**, *6*, 281.
(39) Snyder, R. G. *J. Chem. Phys.* **1967**, *47*, 1316.
(40) Gloaguen, J.-M.; François, P.; Lefebvre, J.-M.; Hue, B. *J. Phys. III (Fr.)* **1994**, *4*, 321.
(41) François, P.; Gaucher, V.; Séguéla, R. *J. Phys., Condens. Matter* **1994**, *6*, 8959.
(42) Nomura, S.; Asanuma, A.; Suehiro, S.; Kawai, H. *J. Polym. Sci., Polym. Phys. Ed.* **1971**, *9*, 1991.
(43) Nomura, S.; Matsuo, M.; Kawai, H. *J. Polym. Sci., Polym. Phys. Ed.* **1972**,*10*, 2489.
(44) Gaucher, V.; François, P.; Séguéla, R. *J. Polym. Sci., Polym. Phys. Ed.*, in press.
(45) Wunderlich, B. *Macromolecular Physics: Crystal Structure, Morphology and Defects* ; Academic Press: New York, 1973; Vol. 1, Chapter 4.
(46) Li, J. C. M. Department of Mechanical and Aerospace Science, University of Rochester, Report COO-2296−3, 1972 (*Chem. Abstr.* **1974**, *81*, 53475n).
(47) Krausz, A. S.; Eyring, H. *Deformation Kinetics*; Wiley-Interscience: New York, 1975.
(48) G'Sell, C.; Jonas, J. J. *J. Mater. Sci.* **1981**, *16*, 1956.
(49) Séguéla, R.; Rietsch, F. *J. Mater. Sci.* **1988**, *23*, 415.
(50) Haward, R. N. *Macromolecules* **1993**, *26*, 5860.
(51) Mansfield, M.; Boyd, R. *J. Polym. Sci., Polym. Phys. Ed.* **1978**, *16*, 1227.
(52) Escaig, B. *Polym. Eng. Sci.* **1984**, *24*, 737.
(53) Friedel, J. *Alliages et Métaux Amorphes*, 21ème colloque de Métallurgie, Inst. Nat. Sc. Tech. Nucl., Saclay Pub., Gif-sur-Yvette, France, pp 59−96.

MA9601878